

Cauchy-perturbative matching and outer boundary conditions: computational studies

Luciano Rezzolla^{a,b}, Andrew M. Abrahams^{a,c}, Richard A. Matzner^d, Mark E. Rupright^e and Stuart L. Shapiro^{a,f,b}

^a*Department of Physics, University of Illinois at Urbana-Champaign, Urbana, Illinois 61801*

^b*NCSA, University of Illinois at Urbana-Champaign, Urbana, Illinois 61801*

^c*J. P. Morgan, 60 Wall St., New York, New York 10260*

^d*The University of Texas at Austin, Austin, Texas, 78712*

^e*Department of Physics and Astronomy, University of North Carolina, Chapel Hill, North Carolina 27599-3255*

^f*Department of Astronomy, University of Illinois at Urbana-Champaign, Urbana, Illinois 61801*

(September 6, 2021)

We present results from a new technique which allows extraction of gravitational radiation information from a generic three-dimensional numerical relativity code and provides stable outer boundary conditions. In our approach we match the solution of a Cauchy evolution of the nonlinear Einstein field equations to a set of one-dimensional linear equations obtained through perturbation techniques over a curved background. We discuss the validity of this approach in the case of linear and mildly nonlinear gravitational waves and show how a numerical module developed for this purpose is able to provide an accurate and numerically convergent description of the gravitational wave propagation and a stable numerical evolution.

PACS numbers: 04.70.Bw, 04.25.Dm, 04.25.Nx, 04.30.Nk

I. INTRODUCTION

In the past few years a considerable effort has been devoted to the solution of Einstein’s equations in numerical simulations of strong-field, highly dynamical sources of gravitational radiation. This effort is partly motivated by the development and construction of gravitational wave detectors such as LIGO, VIRGO, GEO and TAMA. Knowing the theoretical waveform produced by the most likely astrophysical sources of gravitational radiation will not only increase the probability of a successful detection but, most importantly, will allow for the extraction of astrophysically significant information from the observations.

The Binary Black Hole “Grand Challenge” *Alliance* [1], is a major example of this effort, in which a multi-institutional collaboration in the United States was created in order to study the inspiral and coalescence of a binary black hole system, one of the most significant source of signals for the interferometric gravity wave detectors. Present three-dimensional (3D) numerical relativity simulations face a number of fundamental and in some cases unsolved problems, including: coordinate choice, most suitable form of Einstein’s equations, singularity avoiding techniques, gravitational wave extraction and outer boundary conditions. While a robust solution to the generic problem is still awaited, some interesting results have already been obtained, for instance, in the evolution of a generic 3D black hole [2], in the translation of a 3D black hole across a numerical grid [3], and in the extraction of gravitational wave information and imposition of outer boundary conditions [4].

Determining the asymptotic form of the gravitational waves produced in a dynamical evolution of Einstein’s equations is an important goal of many numerical relativity simulations. This goal, however, necessarily requires accurate techniques which compute waveforms from numerical relativity simulations on 3D spacelike hypersurfaces with finite extents. In an ideal situation with unlimited numerical resources, the computational domain can extend into the distant wave zone [5], where the geometric optics approximation is valid and the gravitational waves approach their asymptotic form. With present-day computational limitations, however, the outer boundary of typical numerical relativity simulations lies rather close to the highly dynamical and strong-field region where backscatter of waves off curvature can be significant. As a result, additional techniques need to be implemented in order to “extract” such information from the strong-field region and “evolve” it out to a large distance.

In two recent papers [4,6], we have presented a new method for extracting gravitational wave data from a 3D numerical relativity simulation and evolving it out to an arbitrary distant zone. Our method has been developed within the Alliance in order to match a generic full 3D Cauchy solution of nonlinear Einstein’s equations on spacelike hypersurfaces with a linear solution in a region where the waveforms can be treated as perturbations on a spherically symmetric curved background. This “perturbative module” is used not only to extract gravitational wave data from the Cauchy evolution but, at the same time, to impose outer boundary conditions (A parallel development is also underway in the Alliance to match interior Cauchy solutions to exterior solutions on characteristic hypersurfaces [7]). Indeed, while the problem of radiation extraction is important for computing observable waveforms from numerical simulations, imposition of correct outer boundary conditions is essential for maintaining the integrity of the simulations themselves, as incorrect outer boundary conditions are often a likely source of numerical instabilities. One of the most important requirements for any radiation-extraction and outer-boundary module is that it provides for stable evolution of the interior equations and minimizes the spurious (numerical) reflection of radiation at the boundary. This requirement is particularly important for the “Grand Challenge” investigation in which the computations need to be performed on a gravitational wave emission timescale, which is much longer than the orbital one.

In this paper we present the application of our Cauchy-perturbative matching method to a standard testbed: the evolution of 3D linear and mildly nonlinear gravitational waves. The plan of this paper is as follows: in Section II we briefly review the main features of the approach and recall the essential elements of its numerical implementation. We then concentrate on the two major aspects of this work: in Section IV we present the “*short term*” properties of the Cauchy-perturbative matching and show its ability to provide an accurate and numerically convergent approximation to the gravitational waveform that would be observed in the wave zone surrounding an isolated source. In Section V we turn to the “*long term*” properties of our approach and present a number of different implementations which lead to a *stable* numerical evolution, long after the bulk of the gravitational waves have left the computational grid.

II. THE PERTURBATIVE METHOD

As discussed in [6] (hereafter Paper I), the Cauchy-perturbative matching method involves replacing, at least in parts of the 3D numerical domain, the solution of the full nonlinear Einstein’s equations with the solution of a set of simpler linear equations that can be integrated to high accuracy with minimal computational cost.

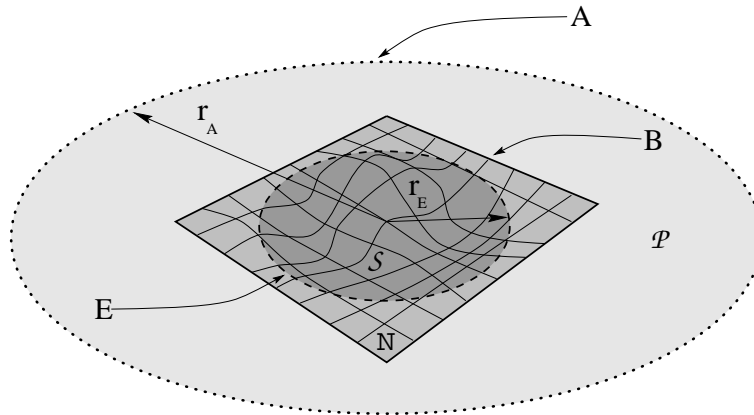


FIG. 1. Schematic picture of the Cauchy-perturbative matching procedure for a spacelike slice of spacetime (one dimension has been suppressed). \mathbf{N} is the 3D numerical grid in which the full Einstein’s equations are solved and \mathbf{B} its 2D outer boundary. The interior (dark shaded) region \mathcal{S} shows the strong-field highly dynamical region of spacetime fully covered by \mathbf{N} . \mathcal{P} is the region of spacetime where a perturbative solution can be performed and extends from the 2-sphere \mathbf{E} (of radius r_E) to the 2-sphere \mathbf{A} (of radius r_A) located in the asymptotically flat region of spacetime. \mathcal{P} is covered entirely by a 1D grid \mathbf{L} (not shown) and partially by the 3D grid \mathbf{N} .

In order to do this, it is necessary to determine the region of spacetime where a perturbative approach can be applied. In general, the 3D numerical grid (indicated as \mathbf{N} in Fig. 1) will comprise an isolated region of spacetime where the gravitational fields are strong and highly dynamical. In this region, indicated as \mathcal{S} in Fig. 1, the full nonlinear Einstein equations must be solved. Outside of \mathcal{S} , however, in what we will refer to as the perturbative region \mathcal{P} , a perturbative approach is not only possible but highly advantageous. Anywhere in the portion of \mathcal{P} covered by \mathbf{N} we can place a two-dimensional (2D) surface which will serve as the surface joining numerically the highly dynamical strong-field region \mathcal{S} and the perturbative one \mathcal{P} . Here, we have chosen this surface to be a 2-sphere of radius r_E , indicated as \mathbf{E} in Fig. 1. It is important to emphasize that the 2-sphere \mathbf{E} *need not* be in a region of spacetime where the gravitational fields are *weak* or the curvature is *small*. In contrast to previous investigations which matched Einstein’s equations onto a Minkowski background [8], the matching is here made on a Schwarzschild background. As a result, the only requirement is that the spacetime outside of \mathcal{S} approaches a Schwarzschild one. Even in the case of a binary black hole merger, it will be possible to find a region of spacetime, sufficiently distant from the binary black holes, where this requirement is met [9–11].

In a practical implementation of the Cauchy-perturbative method, a numerical code provides the solution to the full nonlinear Einstein equations everywhere in the 3D grid \mathbf{N} except at its outer boundary surface \mathbf{B} . At the extraction 2-sphere \mathbf{E} , a different code (i.e. the perturbative module) “extracts” the gravitational wave information and transforms it into a set of multipole amplitudes which we have here chosen to depend only on the radial and time coordinates of the background Schwarzschild

metric (see Paper I and Section II A for details)¹.

In this way, two of the three spatial dimensions of the problem are suppressed and the propagation of gravitational waves on a curved background is reduced to a one-dimensional (1D) problem. During each timestep, information about the gravitational field read-off at \mathbf{E} is propagated by the perturbative module out to the 2-sphere \mathbf{A} in the asymptotic flat region of spacetime. This is done by solving a set of coupled 1D linear differential equations (one for each of the multipoles extracted at \mathbf{E}) on the 1D grid \mathbb{L} (not shown in Fig. 1) covering the perturbative region \mathcal{P} and ranging between r_E and $r_A \gg r_E$. From a computational point of view, this represents an enormous advantage: with a few straightforward transformations, the computationally expensive 3D evolution of the gravitational waves via the nonlinear Einstein equations is replaced with a set of 1D linear equations that can be integrated to high accuracy with minimal computational cost. Although linear, these equations account for all of the effects of wave propagation in a curved spacetime and, in particular, automatically incorporate the effects of backscatter off the curvature (only the wave-wave effects are omitted).

As a result of our construction (and as shown in Fig. 1), the perturbative region \mathcal{P} is entirely covered by a 1D grid \mathbb{L} and only partially by a 3D grid in the complement to \mathcal{S} in \mathbb{N} . The overlap between these two grids is essential. In fact, the knowledge of the solution on \mathcal{P} allows the perturbative module to provide boundary conditions at the outer boundary surface \mathbf{B} and, if useful, Dirichlet data on every gridpoint of \mathbb{N} outside the strong region \mathcal{S} . As we will further discuss in Section V B, this freedom to specify boundary data on a 2-surface of arbitrary shape as well as on a whole 3D region of \mathbb{N} represents an important advantage of the perturbative module over similar approaches to the problem of gravitational wave extraction and imposition of boundary conditions.

A. The basic equations

Our treatment of Schwarzschild perturbation theory is based on the third-order Einstein-Ricci hyperbolic formulation of Einstein field equations [12,13]. A principal advantage of this approach is that gauge-invariant wave equations arise simply from a linear reduction of the full equations without complex changes of variables. Thus, the matching of the perturbative solutions to the fully nonlinear ones becomes rather straightforward. Once the perturbative equations are derived, these are completely general and can be applied to numerical codes solving Einstein's equations in either an explicitly hyperbolic form or, as in the present case, in the standard $3 + 1$ form [14].

We split the gravitational quantities of interest into background parts (denoted by a tilde) and perturbed parts. These are the three-metric $g_{ij} = \tilde{g}_{ij} + h_{ij}$, the extrinsic curvature $K_{ij} = \tilde{K}_{ij} + \kappa_{ij}$, the lapse function $N = \tilde{N} + \alpha$ and the shift vector $\beta^i = \tilde{\beta}^i + v^i$, where the tilde denotes background quantities. Assuming a Schwarzschild background,

$$\tilde{g}_{ij} dx^i dx^j = \tilde{N}^{-2} dr^2 + r^2 (d\theta^2 + \sin^2 \theta d\phi^2), \quad (1)$$

$$\tilde{N} = \left(1 - \frac{2M}{r}\right)^{1/2}, \quad (2)$$

we then have $\tilde{K}_{ij} = 0 = \tilde{\beta}^i$, while the perturbed parts have arbitrary angular dependence.

Using this background, we linearize the hyperbolic equations and reduce the wave equation for K_{ij} to a linear wave equation for κ_{ij} involving also the background lapse [6]. We then separate the angular dependence in this equation by expanding κ_{ij} in terms of tensor spherical harmonics $(\hat{e}_1)_{ij}, \dots, (\hat{f}_4)_{ij}$ [15,16] (we use the notation of [16])

$$\kappa_{ij} = a_{\times}(t, r)(\hat{e}_1)_{ij} + r b_{\times}(t, r)(\hat{e}_2)_{ij} + \tilde{N}^{-2} a_{+}(t, r)(\hat{f}_2)_{ij} + r b_{+}(t, r)(\hat{f}_1)_{ij} + r^2 c_{+}(t, r)(\hat{f}_3)_{ij} + r^2 d_{+}(t, r)(\hat{f}_4)_{ij}, \quad (3)$$

Note that $(\hat{e}_1)_{ij}, \dots, (\hat{f}_4)_{ij}$ are functions of (θ, ϕ) only and, for clarity, angular indices (ℓ, m) for each mode are suppressed. Similarly, the odd-parity multipoles a_{\times} and b_{\times} and the even-parity multipoles a_{+} , b_{+} , c_{+} , and d_{+} also have suppressed indices for each angular mode. There is an implicit sum over all angular modes in (3).

The six multipole amplitudes are not independent. We use the linearized momentum constraints to eliminate the odd-parity amplitude b_{\times} and the even-parity amplitudes b_{+} and c_{+} . As a result, for each (ℓ, m) mode² we obtain one odd-parity equation for a_{\times} :

¹Note that although highly convenient, the suppression of the angular part of the multipoles is not strictly necessary. Indeed, different linear perturbation equations can be derived in which the angular dependence is explicitly contained in the evolution equations.

²Hereafter we will consider only the radiative modes, i.e. those with $\ell \geq 2$

$$\left\{ \partial_t^2 - \tilde{N}^4 \partial_r^2 - \frac{2}{r} \tilde{N}^2 \partial_r - \frac{2M}{r^3} \left(1 - \frac{3M}{2r} \right) + \tilde{N}^2 \left[\frac{\ell(\ell+1)}{r^2} - \frac{6M}{r^3} \right] \right\} (a_{\times})_{\ell m} = 0, \quad (4)$$

and two coupled even-parity equations for a_+ and h :

$$\left[\partial_t^2 - \tilde{N}^4 \partial_r^2 - \frac{6}{r} \tilde{N}^4 \partial_r + \tilde{N}^2 \frac{\ell(\ell+1)}{r^2} - \frac{6}{r^2} + \frac{14M}{r^3} - \frac{3M^2}{r^4} \right] (a_+)_{\ell m} + \left[\frac{4}{r} \tilde{N}^2 \left(1 - \frac{3M}{r} \right) \partial_r + \frac{2}{r^2} \left(1 - \frac{M}{r} - \frac{3M^2}{r^2} \right) \right] (h)_{\ell m} = 0, \quad (5)$$

$$\left[\partial_t^2 - \tilde{N}^4 \partial_r^2 - \frac{2}{r} \tilde{N}^2 \partial_r + \tilde{N}^2 \frac{\ell(\ell+1)}{r^2} + \frac{2M}{r^3} - \frac{7M^2}{r^4} \right] (h)_{\ell m} - \frac{2M}{r^3} \left(3 - \frac{7M}{r} \right) (a_+)_{\ell m} = 0. \quad (6)$$

The independent multipole amplitudes $(a_{\times})_{\ell m}$, $(a_+)_{\ell m}$, $(h)_{\ell m}$ and the corresponding wave equations (4)–(6) for each (ℓ, m) mode are at the basis of the Cauchy-perturbative matching. [Here $(h)_{\ell m}$ is defined in terms of the trace of κ , i.e. $\kappa = (h)_{\ell m} Y_{\ell m}$ where $Y_{\ell m}(\theta, \phi)$ is the standard scalar spherical harmonic.]

B. The basic implementation

As discussed in Section I, with a few straightforward modifications, this method can be applied to a generic 3D numerical relativity code which solves the Cauchy problem of Einstein’s equations in either the standard $3 + 1$ or hyperbolic form. In addition to the standard time integration of the extrinsic curvature K_{ij} and of the spatial metric g_{ij} , three new procedures are performed during each timestep.

(A) The gravitational radiation information contained in K_{ij} and $\partial_t K_{ij}$ is transformed into the independent multipole amplitudes $(a_{\times})_{\ell m}$, $(a_+)_{\ell m}$, $(h)_{\ell m}$ and their time derivatives for all of the relevant (ℓ, m) modes (see Paper I for details). The maximum mode at which the angular decomposition is truncated depends on the basic features of the problem under investigation. However, a simple comparison of the relative amplitudes of the different multipoles it is usually sufficient to provide information about maximum mode necessary.

(B) The values of multipole amplitudes and their time derivatives computed at the extraction 2-sphere on a given timeslice are imposed as inner boundary conditions on the 1D grid \mathbf{L} and evolved [using the radial wave equations (4)–(6) for each (ℓ, m) mode] forward to the following timeslice³ This provides the solution, for the new time level, on the whole perturbative region \mathcal{P} . Since the outer boundary of \mathbf{L} is located, by construction, well out in the wave zone, a simple radial outgoing wave Sommerfeld condition can be imposed there.

(C) From the values at the new time level of $(a_{\times})_{\ell m}$, $(a_+)_{\ell m}$, $(h)_{\ell m}$ and of their time derivatives, it is possible to “reconstruct” the values of K_{ij} or g_{ij} and thus to impose outer boundary conditions on the 3D grid \mathbf{N} . The details of how this is done depend on the formulation of Einstein’s equations solved in \mathbf{N} . In the computations discussed here, we have used the 3D “interior code” of the Alliance [3] adopting an $3 + 1$ formulation of Einstein’s equations. In this case, only the outer boundary data for K_{ij} are necessary, since the interior code can calculate g_{ij} at the outer boundary by integrating in time the boundary values for K_{ij} .

It is important to emphasize the great flexibility of the Cauchy-perturbative approach in providing outer boundary value data. Once again, the ultimate goal is that of providing, during each timestep, boundary values of the relevant quantities at the 2-surface \mathbf{B} delimiting the 3D grid \mathbf{N} . Since we can compute the new values K_{ij} at any point of \mathbf{N} which lies in the perturbative region, not only we can provide boundary data on a 2-surface of arbitrary shape, but, (if necessary) on the the whole portion of \mathbf{N} outside of the extraction 2-sphere \mathbf{E} . This represents a great advantage for which no approximation is required and, as we will discuss in detail in Section V, represents an essential prescription in order to obtain the stability of the code on very long timescales.

III. NUMERICAL SETUP

In Paper I we presented tests of our code based on the propagation of linear waves on a Minkowski background (i.e. with $M = 0$). In those tests, we simulated the Cauchy evolution of the nonlinear interior code by providing an analytic solution on

³Initial data on the 1D grid \mathbf{L} is set consistently with the initial data for the 3D grid \mathbf{N} .

the 3D grid. This was necessary in order to evaluate the accuracy and the convergence properties of the module independently of any error which may develop due to the numerical evolution. As a result of those investigations, we were able to show the module’s ability to extract the gravitational wave information, to evolve this information out to large distances and to impose self-consistent and convergent Dirichlet outer boundary conditions. While extremely useful, those tests could not address a number of important questions which are strictly related to the use of numerical data coming from the solution of the full Einstein’s equations. In particular: (i) what is the influence of the location of the extraction 2-sphere \mathbf{E} on the accuracy of the extracted gravitational wave data? (ii) do Dirichlet boundary conditions on \mathbf{B} provide a long term stability? (iii) what are the most convenient boundary conditions to impose? (iv) are there numerical techniques that would improve the application of the Cauchy-perturbative matching? In this paper we provide an answer to all of these questions and discuss the properties of a Cauchy-perturbative matching in the more realistic study of linear and mildly nonlinear waves.

As in Paper I, we have here computed the propagation of $\ell = 2, m = 0$ (unless otherwise stated) even-parity linear waves, initially modulated by a Gaussian envelope with amplitude $A = 10^{-6}$ and width parameter $b = 1$ [17,18] (Section VI will discuss variations on this type of initial data by using higher ℓ modes and higher amplitudes). Being time-symmetric at the initial time, these waves have ingoing and outgoing parts. At each time level, the extrinsic curvature and 3-metric are computed using the interior code of the Alliance solving the full Einstein’s equations with a geodesic slicing condition (i.e. $N = 1, \beta^i = 0$) on a 3D vertex-centered grid, with extents $(x, y, z) \in [-4, 4]$. The code can provide a solution using either an explicit Leapfrog evolution scheme or a semi-implicit Crank-Nicholson one [19] and we will make explicit reference to which of the two we have used in the different results presented. We have also used a number of different grid resolutions ranging from $(17)^3$ to $(129)^3$ grid points and comparable resolutions have been used on the extraction 2-sphere. In the following Sections we will discuss in the detail the results of our computations and concentrate on two different but interrelated aspects, namely the “short term” and “long term” behaviours. In the first we will consider gravitational wave extraction and imposition of boundary conditions on timescales comparable with the crossing timescale of the numerical grid (i.e. $t \sim 8$). In the second section we consider the opposite regime and investigate the effects of a Cauchy-perturbative matching on time scales much larger than the crossing timescale (i.e. $t \gg 8$) when most of the radiation has left the numerical grid and the stability properties of the module are put to a test.

IV. THE SHORT TERM BEHAVIOUR

As mentioned in [4,6], in the case of a flat background spacetime (as in the present case) and for weak waves on Schwarzschild-like backgrounds, the position of the extraction 2-sphere is arbitrary. This gives us the important possibility of analyzing the influence of the position of the extraction 2-sphere on the accuracy of the gravitational information read-off, and how this then affects the accuracy of the boundary conditions which are provided.

In Fig. 2 we show the timeseries of the multipole amplitude $(a_+)_{20}$ extracted at \mathbf{E} (In the case of an initial traceless $\ell = 2, m = 0$ wave packet this is the only analytically non-zero multipole). Other multipoles of the same mode [e.g. $(a_+)_{21}, (a_+)_{2-1}, (a_+)_{22}, (a_+)_{2-2}$] as well as other parity amplitudes [i.e. $(a_\times)_{\ell m}, (h)_{\ell m}$] are also extracted, but their amplitudes are generally several orders of magnitude smaller. The six different diagrams refer to the six different positions at which we have placed the extraction 2-sphere (i.e. $r_E = 1.0, 1.5, 2.0, 2.5, 3.0, 3.5$). Each diagram also shows the same quantity computed at three different resolutions [namely with $(129)^3, (65)^3$ and $(33)^3$ grid points] and we scale the amplitude by r^3 to compensate for the leading-order radial fall-off of $(a_+)_{20}$.

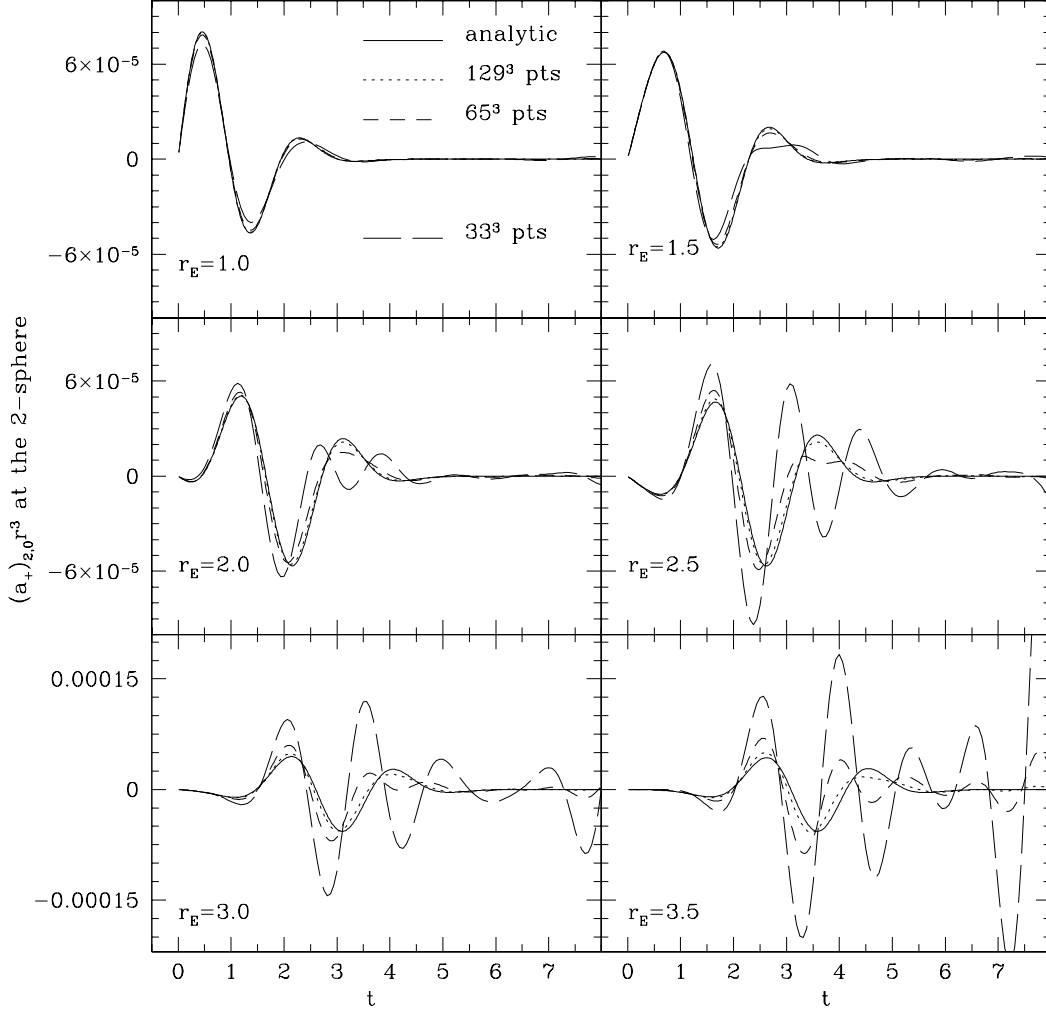


FIG. 2. Timeseries of the multipole amplitude $(a_+)_{20}$ extracted at a 2-sphere of radius $r_E = 1.0, 1.5, 2.0, 2.5, 3.0, 3.5$. Different grid resolutions are indicated with different line types, with a dotted line referring to $(129)^3$ grid points, a short dashed line referring to $(65)^3$ grid points and a long dashed line referring to $(33)^3$ grid points. The analytic solution is indicated with a continuous line. Note that we have scaled the amplitude by r^3 to compensate for the radial fall-off. We have here used a leapfrog integration scheme.

It is clear from Fig. 2 that there is an increasing relative error between the analytic solution and the extracted data as the extraction 2-sphere is placed at larger radii while the resolution is held constant (e.g. compare results at $r_E = 1.0$ and $r_E = 3.5$). Since the results shown in Fig. 2 do not vary if the resolution on the two sphere (i.e. the number of grid points used to cover the extraction 2-sphere) is increased or decreased, the origin of this behaviour has to be found in the intrinsic numerical error which is introduced by the solution of Einstein's equation by the interior 3D code and which becomes larger as the waves propagate outwards. In fact, a more careful investigation of the behaviour of the multipole amplitudes other than $(a_+)_{20}$ shows that the initially traceless linear waves develop a non-zero trace of K_{ij} as the evolution proceeds [The presence of non-zero trace becomes apparent by looking at the amplitudes of the extracted $(h)_{\ell m}$]. A non-zero trace of K_{ij} is due to truncation error and it rapidly converges to zero as the resolution is increased, but it has a subtle effect on the accuracy of the extracted data. While the multipole amplitudes fall approximately as $\sim r^{-3}$, the non-zero trace of K_{ij} remains constant during the time evolution. As a result, for increasing extraction radii, the difference in the amplitudes of say, $(a_+)_{20}$ and $(h)_{20}$, becomes smaller and smaller. For $r_E \gtrsim 3$ the two multipoles are comparable and this error becomes more severe as a coarser resolution is used. However, it is also clear that all of these pathologies can be cured by simply increasing the resolution and Fig. 2 shows the timeseries rapidly converging to the analytic solution as the resolution is increased even in the most extreme case of an extraction radius $r_E = 3.5$. In view of this, we can summarize the properties of the *perturbative radiation extraction* as follows: for any extraction 2-sphere

location, it is always possible to find a resolution for the interior grid which will provide gravitational wave information with the required accuracy.

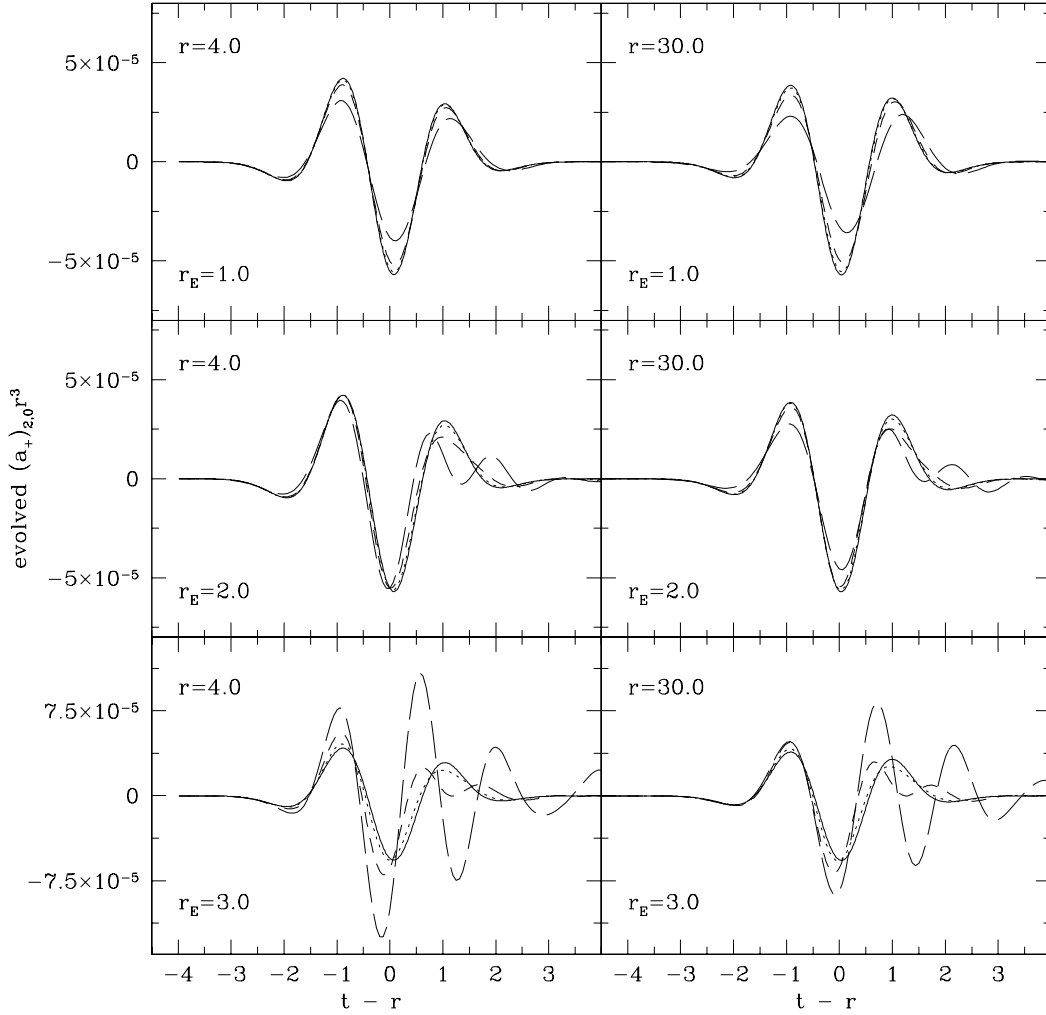


FIG. 3. Timeseries of the multipole amplitude $(a_+)_{20}$ evolved out to a large distance from the center of the grid. The diagrams on the left show values of $(a_+)_{20} r^3$ evolved out to a radius $r = 4.0$ (indicated at the top left corner of each diagram), while the diagrams on the right show values of $(a_+)_{20} r^3$ evolved out to the asymptotic radius $r = 30.0$. We also show data coming from multipoles being extracted at different radii (i.e. $r_E = 1.0, 2.0, 3.0$) and at different grid resolutions. Here also, the amplitude is scaled by r^3 to compensate for the radial fall-off and a leapfrog integration scheme has been used.

Similar considerations apply also for the values of the multipole amplitude $(a_+)_{20}$ which are propagated at large distances from the center of the grid. Fig. 3 shows a set of timeseries of $(a_+)_{20}$ “evolved” out at a radius $r = 4.0$ (indicated at the top left corner of each diagram) corresponding roughly with the outer edge of the 3D grid N and at an asymptotic radius $r = 30.0$. Also in this case, we show data extracted for different positions of the 2-sphere (i.e. $r_E = 1.0, 2.0, 3.0$) and at different grid resolutions. Note that the waveforms evolved at $r = 4.0$ and those at $r = 30.0$ do not differ significantly because at these radii the waveform is dominated by its asymptotic part.

Having shown the the ability of the module to extract convergent gravitational wave data from a fully nonlinear 3D numerical relativity code, we next turn to examine the corresponding ability to “reconstruct” the extrinsic curvature K_{ij} from the information extracted at the 2-sphere (cf. Fig. 2) and evolved out to the asymptotic region (cf. Fig. 3). For the computations discussed in this Section, we have chosen to impose the simplest type of boundary conditions that can be implemented within a Cauchy-perturbative approach. From the solution at the new time level of the evolution equations (4)–(6) for each (ℓ, m) mode

we calculate the value of the extrinsic curvature at all the grid points on \mathbf{B} . We then impose these values as the outer boundary conditions and will refer to this implementation as the *Dirichlet injection* to distinguish it from other types of boundary conditions which will be discussed in the next section.

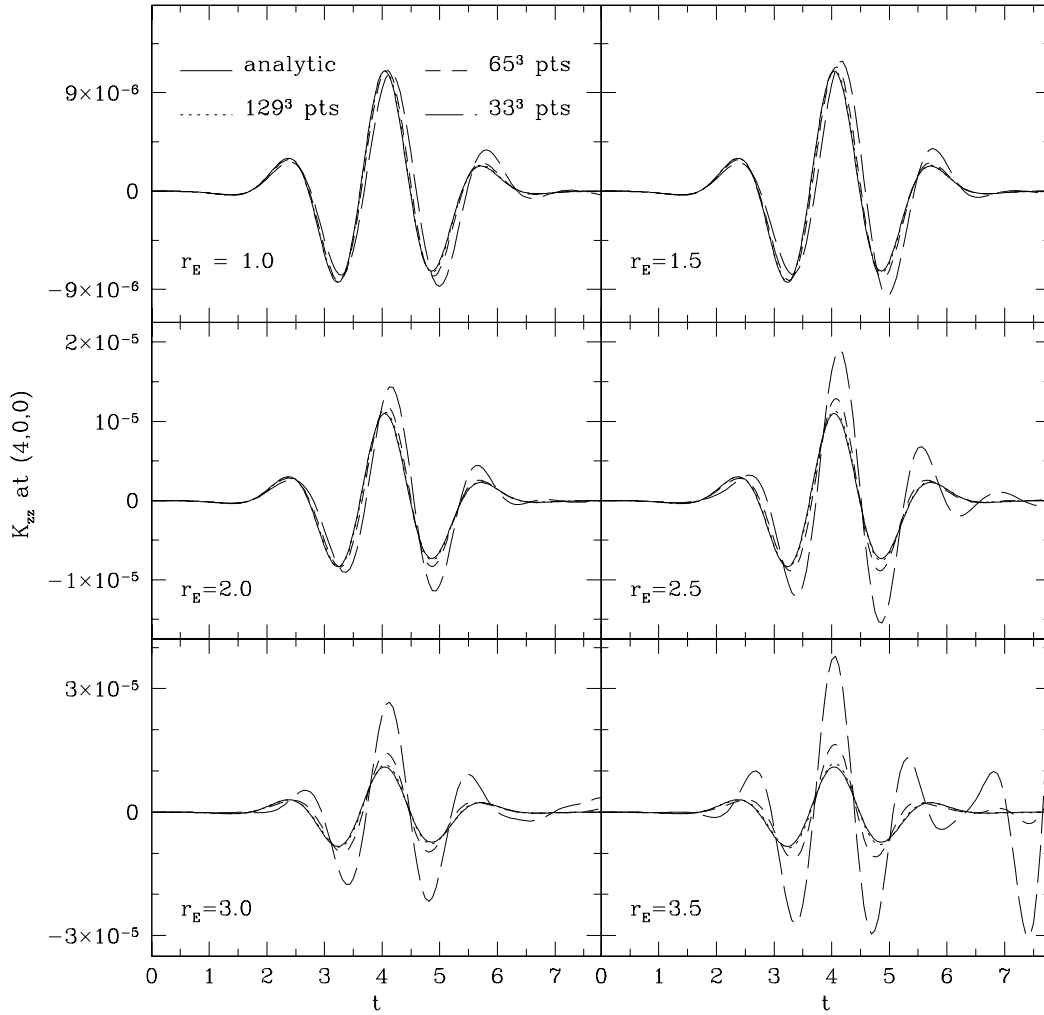


FIG. 4. Timeseries of the reconstructed values of K_{zz} . The six different diagrams refer to the six different positions of the extraction 2-sphere, and for each diagram, results obtained with different grid resolutions are indicated with different line types. The timeseries is computed on a gridpoint at the outer boundary aligned on the x -axis [i.e. at a coordinate location $(4, 0, 0)$] and a leapfrog evolution scheme has been used.

Fig. 4 shows a timeseries of the reconstructed values of the K_{zz} component of the extrinsic curvature for different positions of the extraction 2-sphere and different grid resolutions. The timeseries is computed on a gridpoint at the outer boundary aligned on the x -axis [i.e. at a coordinate location $(4, 0, 0)$]. Equivalent timeseries are shown in Fig. 5 for the K_{yy} component of the extrinsic curvature, which is basically in phase opposition with K_{zz} .

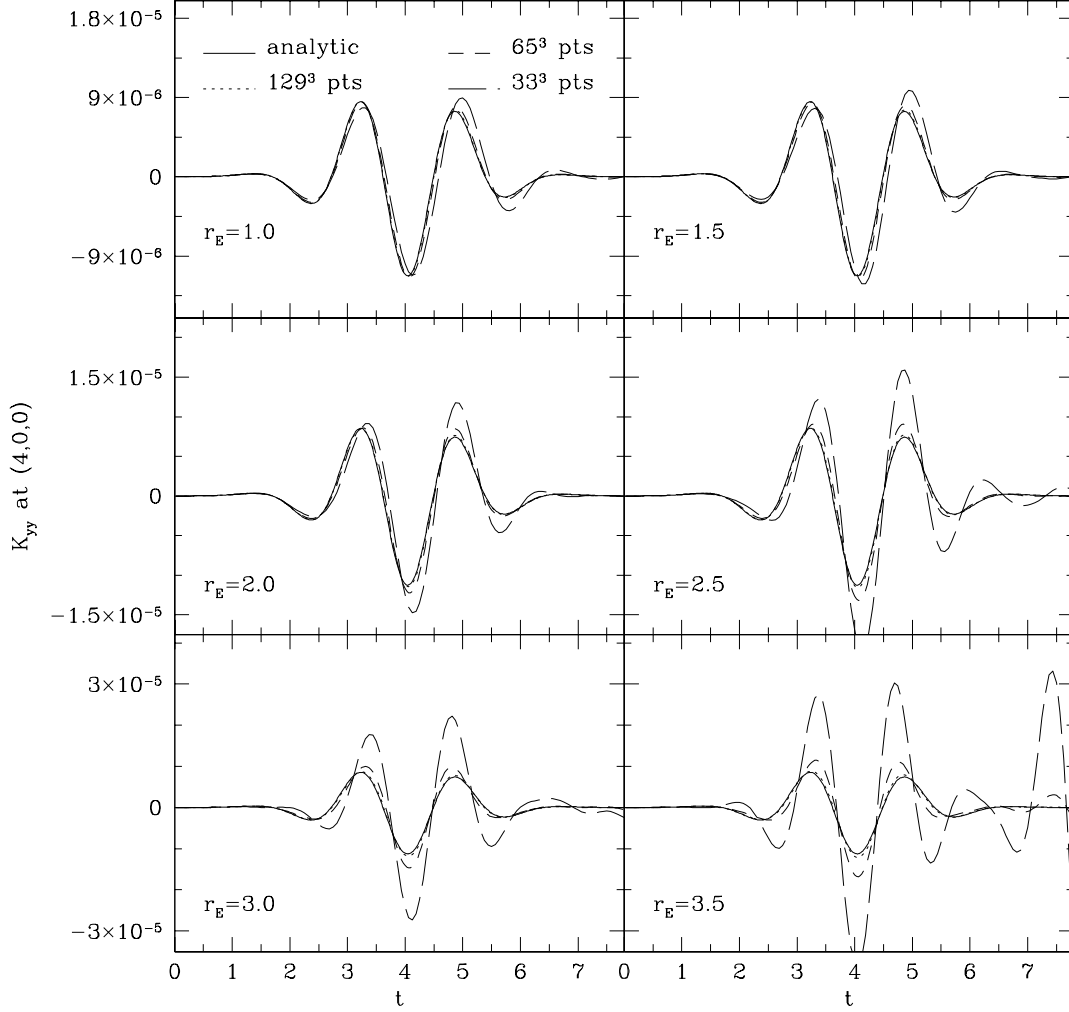


FIG. 5. As in Fig. 4 but for the component K_{yy} of the extrinsic curvature.

It is not surprising that the behaviour of the timeseries for K_{ij} in both Fig. 4 and Fig. 5 mimics the one seen in Fig. 2 and Fig. 3 for the extracted multipole amplitudes. In fact, as we will discuss more in the following section, the extraction 2-sphere and the outer boundary are closely coupled. The accuracy of the boundary conditions imposed is clearly dependent on the accuracy of the extracted gravitational wave information. A large relative error between the extracted and analytic data will translate into a proportionally large relative error between the injected values for K_{ij} and the analytic values for the same quantities.

It is also important to emphasize that the imposition of poor boundary conditions does, in turn, produce spurious reflection of radiation at the outer boundary. This reflected gravitational wave information will contaminate the radiation signal read off at the extraction 2-sphere leading to increasingly larger differences from the purely outgoing analytic solution. In a loose sense, the extraction 2-sphere and the outer boundary behave as a coupled system of microphones and loud-speakers with the 2-sphere playing the role of the microphones. It is clear that such a coupling can be extremely delicate and might be the cause for exponentially growing instabilities as we will discuss in the following Section, where we also indicate a number of prescriptions that make this coupling less important.

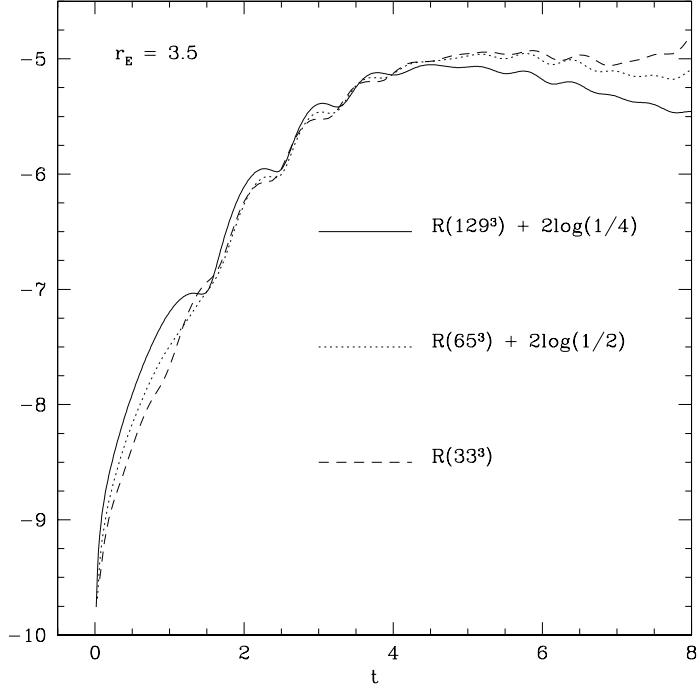


FIG. 6. Logarithm of the L_2 norm of the error in K_{zz} computed over the whole outer boundary \mathbf{B} for successive grid resolutions and for the most unfavorable position of the extraction 2-sphere (i.e. $r_E = 3.5$). The differences between norms at different grid resolutions are normalized by factors $2\log(h_{i+1}/h_i)$, where h_{i+1}, h_i are two successive grid resolutions. The overlap of the curves shows the second-order convergence of the module. The evolution scheme used is leapfrog.

In Fig. 6 we show a more global measure of the accuracy and of the convergence properties for the boundary data by computing the L_2 norm of the error in K_{ij} as measured over the whole 3D outer boundary \mathbf{B} . In particular, in Fig. 6 we plot the L_2 norm of the error in K_{zz} at the outer boundary and for successive grid resolutions (The norms are scaled logarithmically.). Moreover, in order to make the errors comparable, we scale the different curves by numerical factors of the form $2\log(h_{i+1}/h_i)$, where h_{i+1}, h_i are two successive grid resolutions [$(h_{i+1}/h_i) = 1/2$ in these tests]. In order to make this a much more stringent test, we have chosen an extraction radius $r_E = 3.5$. The overlap of the curves is a clear signature of the second-order convergence of the module and of the interior code even when the numerical errors are most severe.

V. THE LONG TERM BEHAVIOUR

Providing an accurate and numerically convergent approximation to the gravitational waveform in the wave zone surrounding an isolated source represents a very important feature of any radiation-extraction and outer-boundary module. However, even more important is that the module provides a stable evolution of the interior equations, minimizing the numerical reflection of radiation at the boundary. Particularly for systems of evolution equations in which radiation and background dominated metric/extrinsic curvature variables are not easily defined, matching techniques may be the only way to achieve a stable evolution. In this section we discuss a number of approaches which were applied to this problem in the context of the Alliance interior evolution code.

A. Perturbative Sommerfeld boundary conditions

The results presented in the previous section were obtained by imposing as outer boundary values for K_{ij} , the ones reconstructed from the values, at the new time level, of the multipole amplitudes. Although straightforward to implement and very accurate, a “Dirichlet injection” of outer boundary data leads to a rapid error growth when the time evolution is carried for sufficiently long periods of time. A careful analysis has revealed that these boundary conditions seem to produce a rather large

amount reflection as the gravitational waves leave the numerical grid. This is basically the result of the slight mismatch between the wave phases and amplitudes imposed at the outer boundary and those in the interior of the 3D numerical grid.

It is clear that a finite discretization will always produce a certain amount of reflection. It is thus important to study and develop new techniques that tend to suppress this reflection and allow, as much as possible, the outgoing radiation to escape freely to infinity. Interesting results in this direction have been obtained implementing a boundary condition we have named *perturbative Sommerfeld* [4]. While a simple Sommerfeld outgoing wave condition applied to a tensor quantity such as the extrinsic curvature or the three metric is (strictly speaking) incorrect, it is often satisfactory, especially if applied in the distant wave zone (cf. [20,21] for the case of linear waves). In view of this, we have related, at the outer boundary \mathbf{B} , the null derivatives of the extrinsic curvature obtained from the interior grid (i.e. K_{ij}) with the one obtained from the perturbative module (κ_{ij} , since background extrinsic curvature is assumed to be zero):

$$\frac{\partial}{\partial t} (K_{ij} - \kappa_{ij}) + \frac{\partial}{\partial r} (K_{ij} - \kappa_{ij}) + \frac{q}{r} (K_{ij} - \kappa_{ij}) = 0, \quad (7)$$

where q is a positive integer⁴. In other words, we “correct” the Sommerfeld outgoing wave condition $\partial_t K_{ij} + \partial_r K_{ij} + (2/r)K_{ij} = 0$, with a right-hand side which is usually taken to be zero but which is not (in general) zero. As a result, this prescription resembles a Sommerfeld condition but is effectively much more general since (i) it can be used in regions where the radiation is not dominated by the asymptotic outgoing behavior and (ii) it takes into account arbitrary angular dependence, as well as the effects of a Schwarzschild black hole background. Since the perturbative correction can be very small and is the result of a near cancelation of several terms involving space and time derivatives, it is important to implement equation (7) so that the same numerical differential operator acts on both K_{ij} and κ_{ij} .

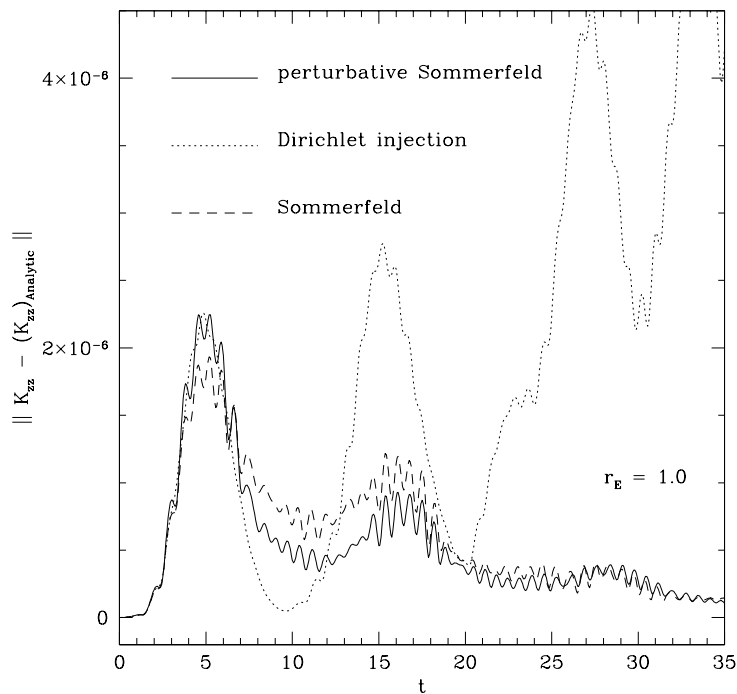


FIG. 7. Timeseries of the L_2 norm of the error in K_{zz} for an extraction at $r_E = 1.0$. The interior code has a resolution of $(33)^3$ grid points and uses a leapfrog integration scheme. The different curves refer to the different types of boundary conditions used.

Implementation of this method has shown that the perturbative Sommerfeld approach is very accurate and generally yields longer evolutions than the direct injection of Dirichlet data. Figure 7 shows a direct comparison of three different boundary

⁴ Results do not depend sensitively on the value of q , which we have chosen to be 2 in these tests in order to reproduce the leading order term in the asymptotic radial fall-off.

conditions, namely, perturbative Sommerfeld, Dirichlet injection and Sommerfeld. In particular, we show the timeseries of the L_2 norm of the error in K_{zz} for an extraction at $r_E = 1.0$. Because we were interested in results over very long times we were forced to perform computations using a very coarse resolution of $(33)^3$ grid points.

There are a number of interesting features that emerge from Fig. 7. The most evident one is strikingly different behaviour between a direct injection of reconstructed data and the use of a Sommerfeld-like boundary condition. In the case of a Dirichlet injection, in fact, not all of the radiation is able to leave the numerical grid, but some of it remains trapped and is repeatedly read-off. In this case the coupling between the extraction 2-sphere and the outer boundary is very strong and amplifies the numerical error which grows exponentially in time, with a beat frequency roughly set by the dimensions of the numerical grid. The perturbative Sommerfeld and the Sommerfeld conditions, on the other hand, are much more effective in letting the radiation escape off the mesh and whatever the amount of reflection, this is progressively damped as the evolution proceeds. In this respect, a perturbative Sommerfeld condition is more efficient in suppressing the reflected incoming radiation (e.g. for $7 \lesssim t \lesssim 17$) and seems to behave basically like a Sommerfeld condition as the evolution progresses further to intermediate times.

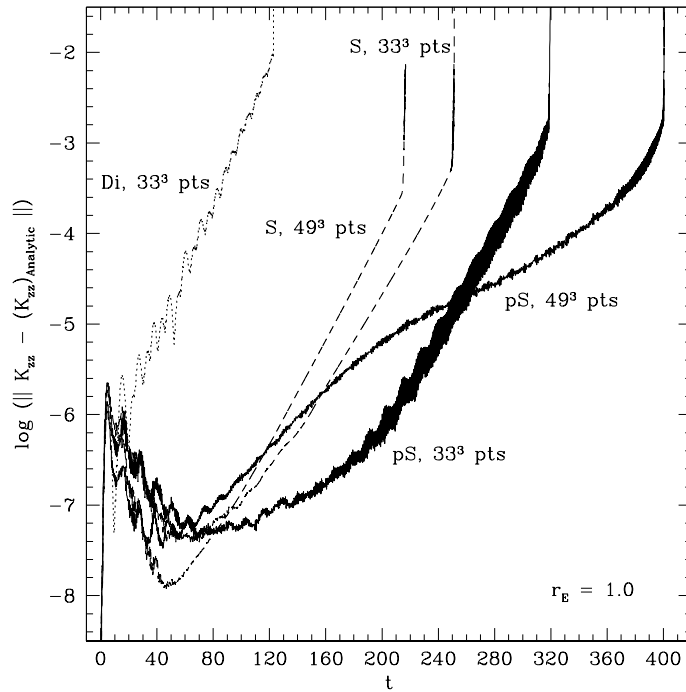


FIG. 8. As in Fig. 7 but for longer timescales and the use of the logarithms of the norms. The different curves refer respectively to Dirichlet injection boundary conditions (Di), Perturbative Sommerfeld boundary conditions (pS) and Sommerfeld boundary condition (S). Curves with a higher resolution of $(49)^3$ grid points are also plotted for the perturbative Sommerfeld and the Sommerfeld boundary conditions. All curves have been obtained with a leapfrog integration scheme.

However, the intrinsically different character of the perturbative Sommerfeld condition becomes apparent on much longer timescales or with higher resolutions. Fig. 8 is the same as Fig. 7 but on a longer timescale. Also, additional curves computed with a resolution of $(49)^3$ grid points are shown for a comparison between the perturbative Sommerfeld and the Sommerfeld condition. While the two types of boundary conditions do not seem to differ significantly and both show the emergence of exponentially growing errors, the use of perturbative boundary conditions delays the onset of the error growth and allows for a much longer evolution. Moreover, by increasing the interior resolution we can further prolong the running time. This is in stark contrast to the behaviour of the Sommerfeld condition, for which an increased interior resolution results in a shorter running time [4]. As shown in Fig. 8, by using $(49)^3$ interior gridpoints, we were able to evolve the code up to $t \sim 400$ and about four times longer than for the case of Dirichlet injection. This is a comparatively very long timescale, which is more than 50 times longer than the physically relevant one, i.e. the crossing timescale.

At present, it is not clear what is the origin of the exponential error growth observed in Fig. 7 and which appears also with evolutions using a harmonic slicing of spacetime. Such instabilities might be directly related to a nonlinear coupling between waves reflected off the outer boundary and numerical instabilities triggered by the $3 + 1$ form of Einstein's equations. It is indeed remarkable that no exponential growth is present in other formulations of Einstein's equations, such as the one proposed

by Shibata and Nakamura or the Einstein-Ricci hyperbolic formulation, in which linear waves have been stably evolved in harmonically sliced spacetimes [22,23].

B. Perturbative boundary conditions with “blending”

The perturbative Sommerfeld boundary conditions represent a very promising implementation of the Cauchy-perturbative matching and provide both high accuracy and very small reflection at the outer boundary. Despite these appealing features, they do not provide for very long term stability of the interior code and, as shown in Fig 8, they eventually suffer from an exponential growth. Of course, in the computations reported here, the boundary conditions provided by the Cauchy-perturbative matching are totally adequate on the timescale necessary for the gravitational waves to leave the numerical grid. Indeed, the instabilities induced by the outer boundary become relevant only long after the crossing timescale, when the grid basically contains numerical noise. However, providing accurate boundary conditions on a dynamical timescale is usually not sufficient and the achievement of unconditionally stable codes is not only of academic interest. In order to successfully model the problem of binary black hole coalescence, the numerical code will have to be able to stably solve Einstein’s equations on a timescale (the gravitational wave emission one) which is much longer than the dynamical one. It is therefore imperative to devise a technique which provides unconditionally stable boundary conditions. A first successful step in this direction has been made with the implementation of the “perturbative-blending” technique we will discuss in this Section.

As discussed in the previous Section, the perturbative Sommerfeld boundary conditions are much more effective in providing accuracy and reducing reflection at the outer boundary than is the simple Dirichlet injection. One of the major differences between the two types of boundary conditions is in their numerical implementation. This involves only the outermost boundary grid points (i.e. those on \mathbf{B} of Fig. 9) in the case of a Dirichlet injection but also the closest interior neighbouring gridpoints in the case of a perturbative Sommerfeld condition [necessary for taking a finite difference form of the spatial derivatives in (7)]. The perturbative blending can then be considered as the extension of the perturbative Sommerfeld condition to a larger set of gridpoints. The basic idea is simple and based on the attempt of modifying the propagation characteristics in the vicinity of the outer boundary with the goal of acting distinctively on the outgoing and ingoing parts of the gravitational waves. A detailed description of the basic properties of “sponge filters” in conjunction with absorbing boundary conditions in one-dimensional wave propagation can be found in [24] and results of its application are also discussed in [25]. The interpretation of the blending as an implementation of the sponge filter method will be given in Appendix A.

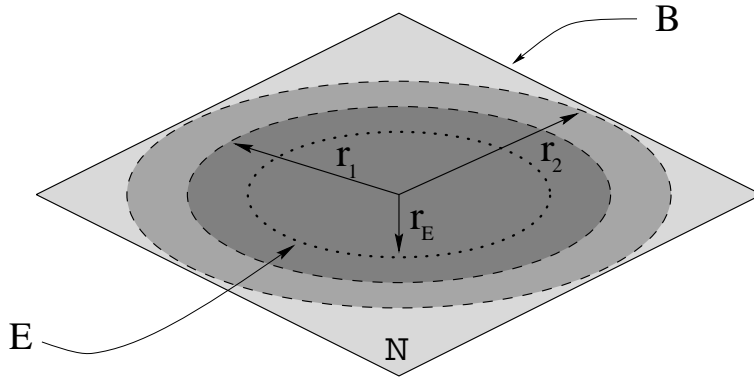


FIG. 9. Schematic of the numerical implementation of a “perturbative blending” matching. As in Fig. 1, \mathbf{N} represents the 3D numerical grid in which the full Einstein’s equations are solved and \mathbf{B} its 2D outer boundary. r_E is the radius of the extraction 2-sphere \mathbf{E} and r_1, r_2 are two radii chosen so that $r_2 > r_1 > r_E$. The dark shaded region (i.e. $r < r_1$) shows the portion of \mathbf{N} filled by the numerical nonlinear solution provided by the interior code. The medium shaded region (i.e. $r_2 < r < r_1$) shows the portion of \mathbf{N} in which the solution of the interior code is “blended” with the one coming from the linearized Einstein’s equations. Finally, in the light shaded region, only the perturbative solution is used.

Figure 9 gives a schematic representation of the way the perturbative blending has been implemented. The key feature of this specific approach comes from exploiting the module’s ability to provide a perturbative solution to Einstein’s equation not only on the outer boundary \mathbf{B} but, in principle, in the whole region of the 3D numerical grid \mathbf{N} outside of the extraction 2-sphere

E. However, rather than doing this, we have isolated a spherical shell of radii r_1 and r_2 (where $r_2 > r_1 > r_E$) and blended therein the nonlinear solution coming from the interior code with the linear one coming from the Cauchy-perturbative module (this is shown as the medium shaded region in Fig. 9). In particular, at the end of each time step (as well as during each iteration of the Crank-Nicholson evolution scheme we have used in these tests), we do the following: at all of the gridpoints at $r < r_1$ (dark shaded region in Fig. 9) the nonlinear solution is left unmodified; for all of the gridpoints between r_1 and r_2 we “blend” the nonlinear solution with the perturbative one reconstructed at that grid point; for all of the gridpoints at $r > r_2$ we replace the computed values of K_{ij} with perturbative data. The “blending”, consists of smoothly weighting the nonlinear and linear solutions so that the first one is imposed at the 2-sphere of radius r_1 and the second one is imposed at r_2 (see Appendix A for details).⁵ Stability does not depend on the form of the weighting power function as long as the latter satisfies the boundary conditions of being zero at the inner blending shell and one at the outer blending shell. However, a more careful matching of the first and second derivatives at the two blending shells does provide a smaller amount of reflection off the outer boundary during the initial stages of the evolution (i.e. for $t \lesssim 20$).

Figs. 10 and 11 illustrate the radical changes in the long time behaviour introduced by the use of a perturbative blending match.

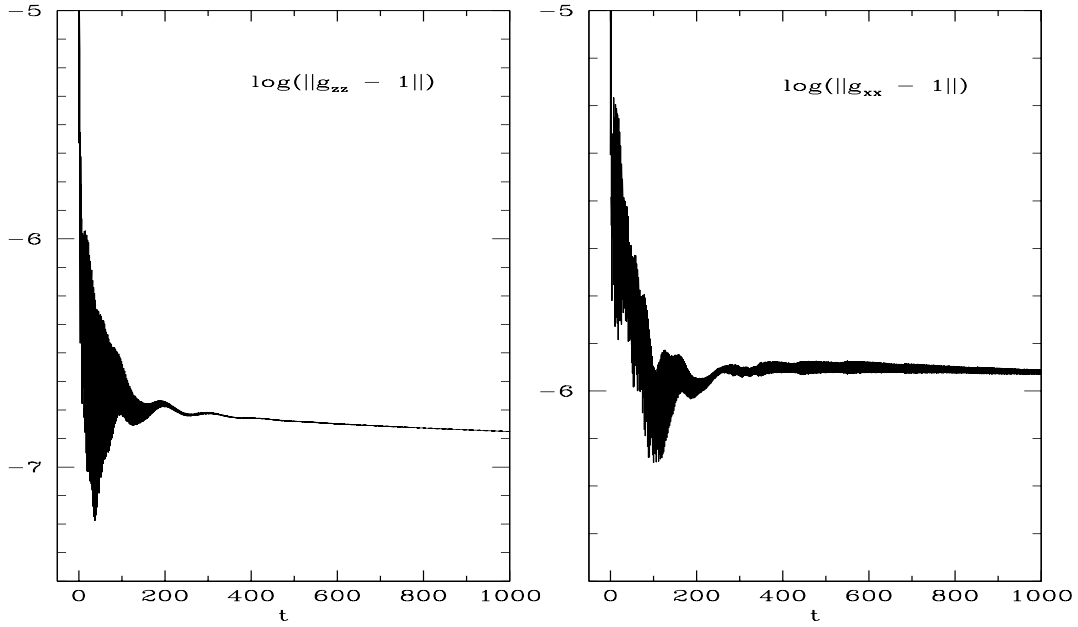


FIG. 10. Timeseries of the errors for the g_{zz} and the g_{xx} components of the three-metric with the use of a perturbative blending match. The norms shown here are taken along the z -axis and not on a 2D surface as for the previous diagrams. In these runs we have used a very coarse resolution of $(33)^3$ gridpoints and an extraction radius $r_E = 1$. The blending region is covered with 10 gridpoints, but similar results have been obtained also with smaller numbers of gridpoints. The integration scheme used is Crank-Nicholson.

In particular, in Fig. 10 we show the timeseries of the errors for the g_{zz} and the g_{xx} components of the three-metric, while in Fig. 11, we show the timeseries of the errors in the K_{zz} component of the extrinsic curvature and of the violation of the Hamiltonian constraint. The plots refer to computations performed using a coarse resolution of $(33)^3$ gridpoints and an extraction radius $r_E = 1$.

⁵The idea of blending boundary conditions was first proposed within the Alliance by R. Gómez and the Pittsburgh group who obtained stable evolution of linear waves after blending the numerical solution with the *analytic* one [26].

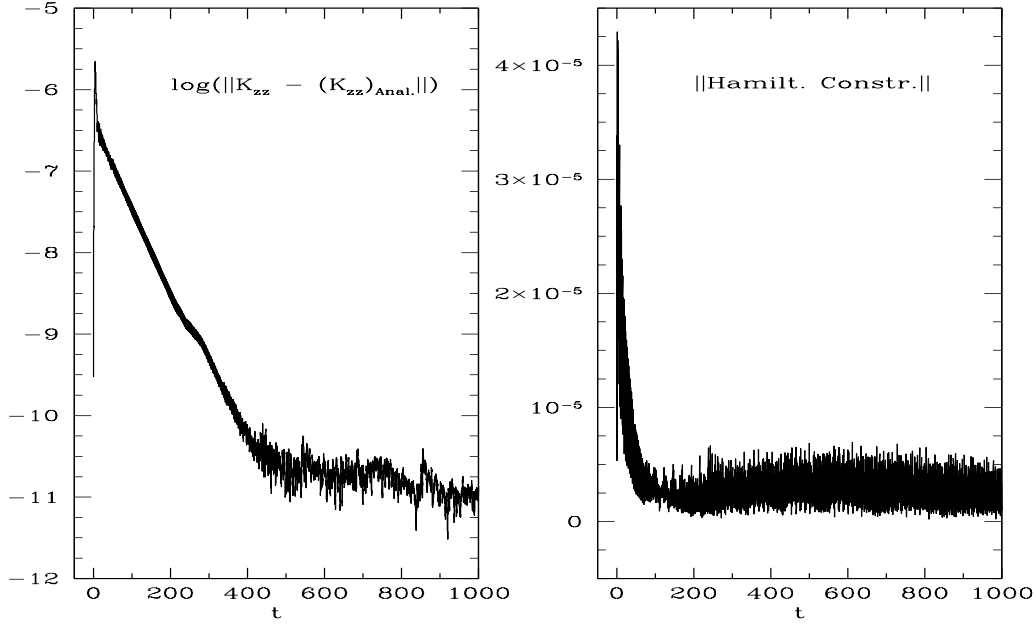


FIG. 11. Timeseries of the errors in the K_{zz} component of the extrinsic curvature and of the violation of the Hamiltonian constraint when a perturbative blending match is used. The resolution is that of $(33)^3$ gridpoints and the extraction radius if $r_E = 1$ and the blending region is covered with 10 gridpoints. The integration scheme used is Crank-Nicholson.

The long evolution times reached and the quiescent behaviour of the evolved variables reduced to their roundoff error values, clearly show that the use of a perturbative blending match does provide the desired long term stability. This is evident from the gradual decay of the norms and the stationary behaviour of the violation of the Hamiltonian constraint which does not show any sign of instability on a timescale more than 125 times the crossing timescale [27]. We have also verified that the perturbative-blending boundary conditions provide *accurate* short term extraction of the waveform, comparable to the results in Figures 2–5.

It is also clear that the use of a perturbative blending introduces two new “free” parameters (i.e. the radii r_1 and r_2) and a satisfactory implementation will therefore depend on some “tuning” and experimentation. In particular, for the runs shown above we have chosen $r_E = 1$, $r_1 = 2$ and $r_2 = 4$, which is the radius of the sphere inscribed in N and tangent to it. This gives about 10 gridpoints along the axes where the blending between the nonlinear and linear solutions is made. Very similar results have been obtained also with 9, 8 and 7 gridpoints, but a blending over 6 or fewer gridpoints would make exponentially growing instabilities reappear. Provided that the intrinsic length of the blending is region is kept constant, stability has been obtained also with simulations using a larger or a coarser resolution than the one shown for in Figs. 10 and 11.

A detailed understanding of the properties of the perturbative blending matching is still under development and is particularly hard to achieve given the three-dimensionality of the full problem. However, there are some basic features that seem to be well established and that we have illustrated in the Appendix. There, using simplified 1D model describing the evolution of linear waves on a flat background, we show that imposing boundary conditions using a mixture of a numerical solution of Einstein’s equations with another one (either analytic or obtained from a perturbative matching) is equivalent to imposing a variable phase velocity in the zone where the blending is made. If appropriate boundary conditions are applied to this variable phase velocity, the blending can tilt the ingoing characteristic toward the advected one and prevent ingoing modes propagating from the outer boundary. Moreover, the blending progressively dampens the propagation of outgoing modes which are totally absorbed at the outer boundary. In this way, it is possible to decouple the outer boundary from the interior evolution without having to place it at very large distances (see the Appendix for details).

The use of perturbative blending boundary conditions has provided the unconditional long-term stability we were requiring to our radiation-extraction and outer-boundary module. Given the versatility of the perturbative matching, this approach could represent a very powerful tool also in other numerical relativity applications. Further work is necessary in this direction and experimentation with more complex physical configurations. It is interesting to note that Gómez’s original prescription of blending numerical and analytic data has found a partially successful application also in the 3D Cauchy evolution of a single black hole where it lead to the first stable evolution [28] of this type.

VI. VARIATIONS ON THE THEME: HIGH MODE AND MILDLY NONLINEAR WAVES

In this concluding Section we provide further evidence of the robustness and versatility of the Cauchy-perturbative matching in extracting gravitational wave information and providing outer boundary conditions. For this purpose we present results obtained from computations having different initial data than the one discussed so far and concentrate on short term evolutions.

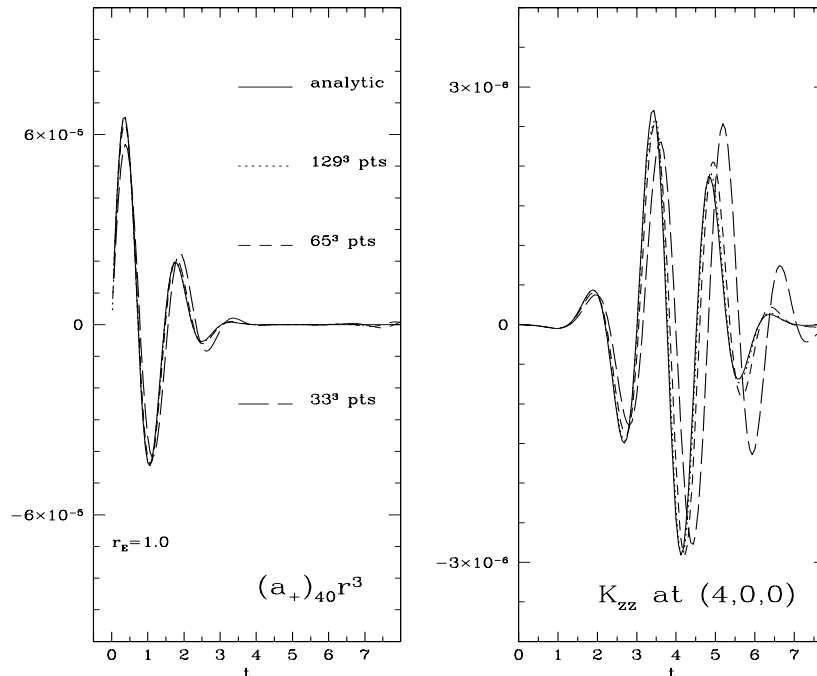


FIG. 12. The left diagram shows the timeseries of the multipole amplitude $(a_+)_{40}$ extracted at a 2-sphere of radius $r_E = 1.0$ for different grid resolutions (cf. Fig. 2). The right diagram, the timeseries of the reconstructed values of K_{zz} as measured at the gridpoint $(4,0,0)$ (cf. Fig. 4).

In particular, in Fig. 12 we show the extracted signal (left diagram) and the injected boundary conditions for K_{zz} (left diagram) when an initial $\ell = 4$, $m = 2$ even-parity wave is used as initial data (We have here maintained the same amplitude $A = 10^{-6}$ and width parameter $b = 1$; note also that we have used the Crank-Nicholson evolution scheme.) Fig. 12 should be compared with Figs. 2 and 4 where similar data is reported in the case of an initial $\ell = 2$, $m = 0$ packet. It seems evident that also in the case of this higher mode initial data the Cauchy-perturbative module is able to provide convergent wave extraction and boundary conditions (For this test and the following ones in this Section, we have used the computationally less expensive perturbative Sommerfeld boundary conditions.)

Next, we can consider the behaviour of the module when the initial amplitude of the wave packet is increased. Of course, the analytic form for the initial data used in these tests is derived in the linearized regime and a wave packet with an exceedingly large amplitude will no longer satisfy the Hamiltonian and momentum constraints. However, we can progressively increase the initial amplitude and exclude amplitudes above which the violation of the constraints becomes too severe (e.g. more than 50%). This allows us to perform an interesting check of the efficiency of the module in the linear and mildly nonlinear regime.

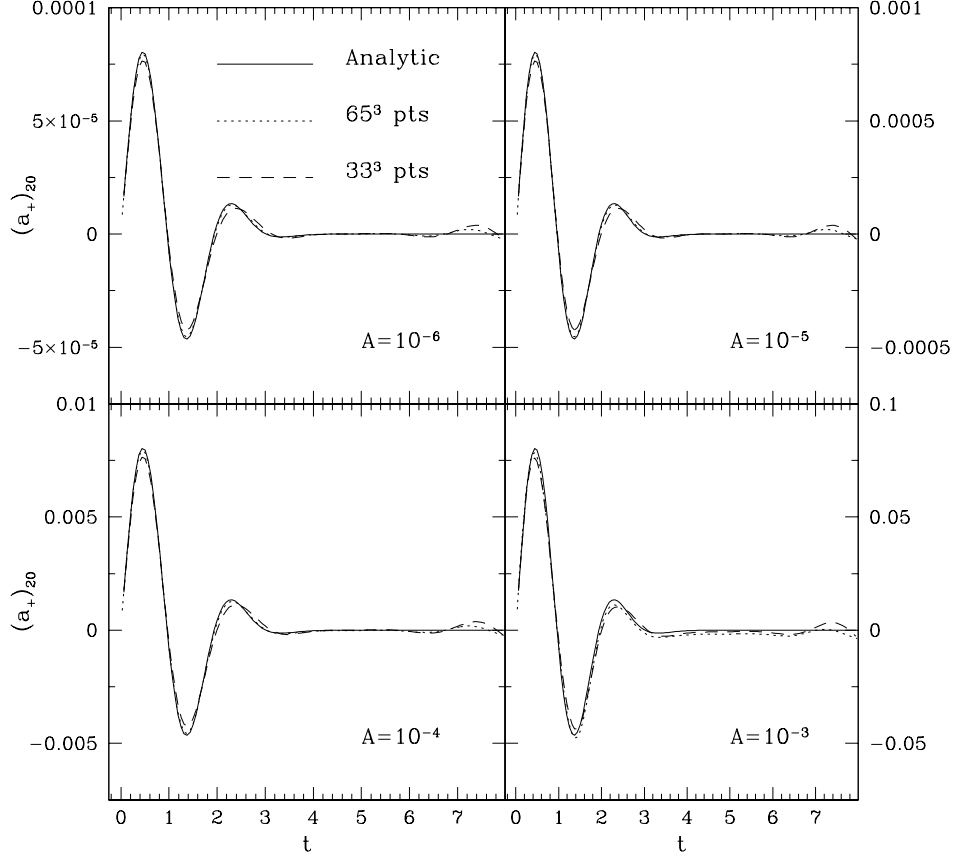


FIG. 13. Timeseries of the multipole amplitude $(a_+)_{20}$ extracted at a 2-sphere of radius $r_E = 1.0$ for different values of the initial wave amplitude (i.e. $A = 10^{-6} - 10^{-3}$). Different grid resolutions are indicated with different line types (cf. Fig. 2). The integration scheme used is Crank-Nicholson.

Results of these tests are presented in Figs. 13 for the extraction of gravitational waves and in Fig. 14 for the imposition of outer boundary conditions (for these tests we have gone back to the less computationally expensive $\ell = 2, m = 0$ initial wave packet). Fig. 13, in particular, shows the timeseries of the multipole amplitude $(a_+)_{20}$ extracted at a 2-sphere of radius $r_E = 1.0$ for amplitudes ranging from $A = 10^{-6}$ to $A = 10^{-3}$. It is interesting to note how all diagrams are almost perfectly identical but for the different scale used. Similar considerations apply also for the boundary conditions imposed at the outer boundary and shown for the zz component of the extrinsic curvature in Fig. 14

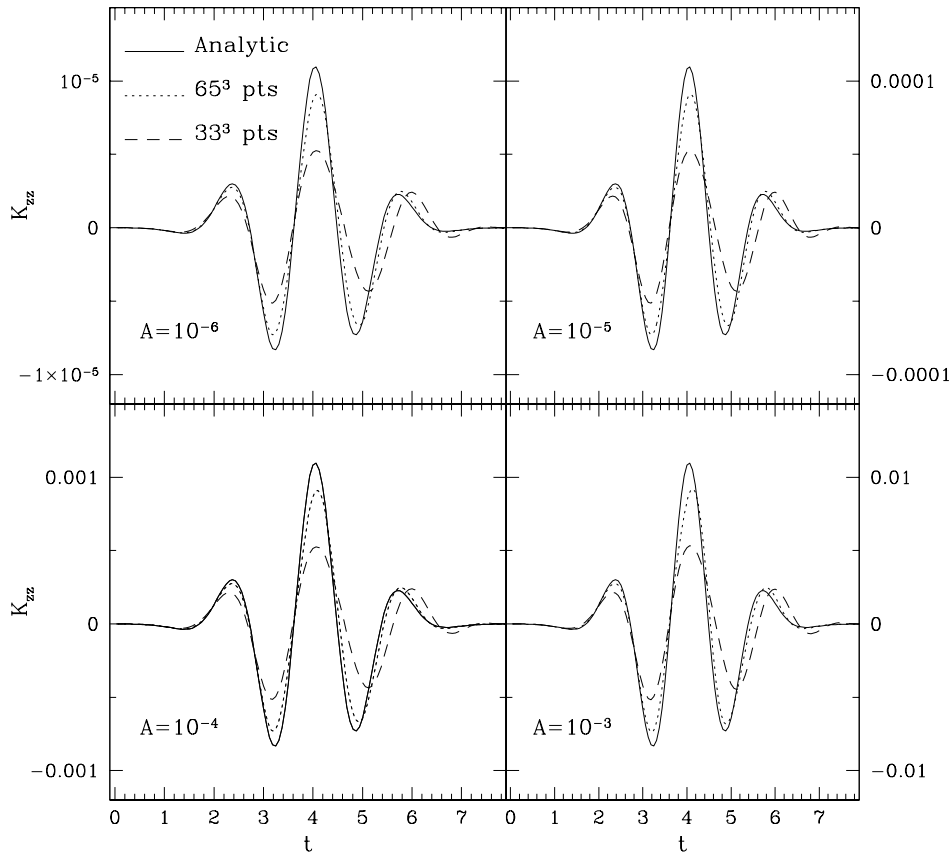


FIG. 14. Timeseries of the reconstructed values of K_{zz} as measured at the gridpoint (4,0,0). The four different diagrams refer to the four different amplitudes used for the initial wave amplitude (i.e. $A = 10^{-6} - 10^{-3}$, cf. Fig. 4, Fig. 13). The integration scheme used is Crank-Nicholson.

VII. CONCLUSION

We have investigated the properties of the Cauchy perturbative method for matching gravitational data computed from a 3D Cauchy solution of Einstein field equations. Studying the evolution of linear and mildly nonlinear waves we have shown the ability of the perturbative module to extract convergent gravitational wave information at different locations within the 3D numerical grid solving the nonlinear form of Einstein's equation. We have shown that, given an extraction 2-sphere radius, a resolution can be found which provides extraction and reinjection with the required accuracy.

We have also discussed in detail a number of different approaches to the problem of imposing outer boundary conditions. Relying on the important advantage of being able to provide information on the whole portion of the 3D numerical grid outside the extraction 2-sphere, we have investigated Dirichlet boundary conditions, perturbative Sommerfeld boundary conditions and "perturbative blended" boundary conditions. Each of these approaches has been shown to provide convergent boundary conditions, but only the latter provides stable evolutions. It has been recognized for sometime that it is advantageous to make variable choices for numerical relativity which separate those variables with dominantly wavelike character from those dominated by static/stationary field moments ([29,30,8,31,22]). In the tests presented here, the perturbative module provided a brute-force imposition of this separation and, with suitable numerical implementation, enabled long-term stability.

These first successes of Cauchy perturbative matching method motivate further work in this direction, both in the application of our numerical module to fully nonlinear spacetimes and in the extension of the mathematical apparatus to more general background spacetimes.

ACKNOWLEDGMENTS

It is a pleasure to thank Roberto Gómez, Jeff Winicour, Thomas Baumgarte and Matt Choptuik for helpful discussions and suggestions. We are also grateful to Greg Cook, Mijan Huq, Scott Klasky and Mark Scheel for providing the interior evolution code. This work was supported by the NSF Binary Black Hole Grand Challenge Grant Nos. NSF PHY 93–18152, NSF PHY 93–10083, ASC 93–18152 (ARPA supplemented) and by the NSF Grant AST 96–18524 to the University of Illinois at Urbana-Champaign. Computations were performed at NPAC (Syracuse University) and at NCSA (University of Illinois at Urbana-Champaign).

APPENDIX A: TOY MODEL FOR BLENDING BOUNDARY CONDITIONS

The very simplest model for investigating and interpreting the effects of perturbative blending boundary conditions is provided by linearized gravity waves in one dimension. The dynamical equations can be written symbolically as

$$\dot{\mathbf{g}} \equiv \partial_t \mathbf{g} \sim -\mathbf{K} , \quad (\text{A1})$$

$$\dot{\mathbf{K}} \sim -\mathbf{g}'' \equiv -\partial_x^2 \mathbf{g} , \quad (\text{A2})$$

where \mathbf{g} and \mathbf{K} are the fully nonlinear three-metric and extrinsic curvature tensors respectively, whose numerical solution is provided by the interior code. The blending condition on the extrinsic curvature within the blending region can then be expressed as

$$\mathbf{K}_B \equiv a(x)\mathbf{K} + [1 - a(x)]\mathbf{K}_{pert} \quad (\text{A3})$$

where $a(x)$ is the “blending function”, continuous in the range $x \in [x_1, x_2]$ and defined so that $a(x_1) = 1$ (i.e. at the inner edge of the blending layer) and $a(x_2) = 0$ (i.e. at the outer edge of the blending layer). \mathbf{K}_{pert} could be the perturbative solution of Einstein’s equations in the blending region (Note that the following arguments will not depend on \mathbf{K}_{pert} being a perturbative solution. In fact, in Gómez’s first application of the blending boundary conditions, \mathbf{K}_{pert} was the value given by an analytic solution [26].)

Applying the boundary condition (A3) then yields

$$\dot{\mathbf{g}}_B \sim -\mathbf{K}_B \sim -a(x)\mathbf{K} - [1 - a(x)]\mathbf{K}_{pert} , \quad (\text{A4})$$

and therefore

$$\ddot{\mathbf{g}}_B \sim a(x)\mathbf{g}'' - [1 - a(x)]\dot{\mathbf{K}}_{pert} . \quad (\text{A5})$$

In the simplest case in which the perturbative value for the extrinsic curvature is zero, the result of the blending is then a wave equation (in this case, in fact, $\mathbf{g}'' = \mathbf{g}''_B$) with a variable phase propagation speed, $v_p^2(x) = a(x)$, which is unity at the inner radius of the blending region and “smoothly” (in a discretized sense) goes to zero at the outer edge of the blending region:

$$\ddot{\mathbf{g}}_B \sim a(x)\mathbf{g}'' . \quad (\text{A6})$$

A less trivial and more interesting case is the one in which an outgoing Sommerfeld condition is imposed within the blending region. In this case:

$$\mathbf{g}' \sim -\dot{\mathbf{g}} \sim \mathbf{K}_{pert} , \quad (\text{A7})$$

and the “blended” equivalents of equations (A1) and (A5) are

$$\dot{\mathbf{g}}_B = -a(x)\mathbf{K} - [1 - a(x)]\mathbf{g}' , \quad (\text{A8})$$

$$\ddot{\mathbf{g}}_B \sim -a(x)\dot{\mathbf{K}} - [1 - a(x)]\dot{\mathbf{g}}' \sim a(x)\mathbf{g}'' - [1 - a(x)]\dot{\mathbf{g}}' . \quad (\text{A9})$$

Consider now an outgoing packet so that $\mathbf{g} \propto \text{const} \times e^{i(\omega t - kx)}$ and similarly for \mathbf{g}_B . The dispersion relation following from (A9) will be then

$$\omega^2 - (1 - a)k\omega + ak^2 = 0 , \quad (\text{A10})$$

whose solutions are

$$v_p(x) = \frac{\omega(x)}{k(x)} = \frac{[1 - a(x) \pm (1 + a(x))]}{2} = (1, -a(x)). \quad (\text{A11})$$

As a result, the wave packet will have unit outgoing and ingoing phase velocities at the inner edge of the blending region, decreasingly smaller ingoing phase velocities in the blending region and only outgoing phase velocity at the outer edge of the blending region and outside of it.

Finally, it can be seen that the blending approach, especially the blending to the Sommerfeld condition, just described, has a close relation to the techniques described in reference [24]. However, for the strongly nonlinear black hole simulations, the more manageable approach of blending with *analytic solutions*, as in the first example above, has been successful in some cases [28]. This method is computationally much simpler than explicitly modifying the equations.

- [1] Information about the Binary Black Hole Grand Challenge Alliance, its goals and present status of research can be found at the web page: <http://www.npac.syr.edu/projects/bh/>.
- [2] The Grand Challenge Alliance: R. Gómez, L. Lehner, R. L. Marsa, J. Winicour *et al.*, Phys. Rev. Lett. **80**, 3915 (1998).
- [3] The Grand Challenge Alliance: G. B. Cook, M. F. Huq, S. A. Klasky, M. A. Scheel *et al.*, Phys. Rev. Lett. **80**, 2512 (1998).
- [4] The Grand Challenge Alliance: A. M. Abrahams, L. Rezzolla, M. E. Rupright *et al.*, Phys. Rev. Lett. **80**, 1812 (1998).
- [5] K. S. Thorne, Rev. Mod. Phys. **52**, 299 (1980).
- [6] M. E. Rupright, A. M. Abrahams and L. Rezzolla, gr-qc/9801000, Phys. Rev. D. *in press*.
- [7] N. T. Bishop, R. Gómez, P. R. Holvorcem, R. A. Matzner, P. Papadopoulos and J. Winicour, Phys. Rev. Lett. **76**, 4303 (1996); N. T. Bishop, R. Gómez, L. Lehner, J. Winicour, Phys. Rev. D. **54**, 6153 (1996).
- [8] A. M. Abrahams and C. R. Evans, Phys. Rev. D, **37**, 317 (1988); Phys. Rev. D, **42**, 2585 (1990).
- [9] R. H. Price and J. Pullin, Phys. Rev. Lett. **72**, 3297 (1994).
- [10] A. M. Abrahams and G. Cook, Phys. Rev. D **50**, 2364(1994).
- [11] A. M. Abrahams, S. L. Shapiro and S. A. Teukolsky, Phys. Rev. D **51**, 4295 (1995); A. M. Abrahams and R. H. Price, Phys. Rev. D **53**, 1963, *Ibidem*, 1972 (1996).
- [12] Y. Choquet-Bruhat and J. W. York Jr., C. R. Acad. Sci. Paris **321**, 1089 (1995).
- [13] A. M. Abrahams, A. Anderson, Y. Choquet-Bruhat, and J. W. York Jr., Phys. Rev. Lett. **75**, 3377 (1995).
- [14] J. W. York Jr. in *Sources of Gravitational Radiation*, edited by L. Smarr, Cambridge Univ. Press, Cambridge (1979).
- [15] T. Regge and J.A. Wheeler, Phys. Rev. **108**, 1063 (1957)
- [16] V. Moncrief, Ann. Phys. **88**, 323 (1974).
- [17] W. L. Burke, J. Math. Phys. **12**, 401 (1971).
- [18] S. A. Teukolsky, Phys. Rev. D **26**, 745 (1982).
- [19] W. H. Press, B. P. Flannery, S. A. Teukolsky and W. T. Vetterling, *Numerical Recipes*, Cambridge University Press, Cambridge (1986).
- [20] L. Rezzolla, A. M. Abrahams, T. W. Baumgarte, G. B. Cook, M. A. Scheel, S. L. Shapiro and S. A. Teukolsky, Phys. Rev. D **57**, 1084 (1998).
- [21] G. B. Cook, M. F. Huq, S. A. Klasky, M. A. Scheel, Proceedings of “The Grand Challenge Alliance Spring Meeting”, Penn State University, April 1997.
- [22] M. Shibata and T. Nakamura, Phys. Rev. D **52**, 5428 (1995).
- [23] G. B. Cook and M. A. Scheel, *private communication*.
- [24] M. Israeli and S. A. Orszag, Journ. Comp. Phys. **41**, 115 (1981).
- [25] R. L. Marsa and M. W. Choptuik, Phys. Rev. D **54**, 4929 (1996).
- [26] R. Gómez, Proceedings of “The Grand Challenge Alliance Fall Meeting”, Los Alamos, October 1997; Newsletter of the Grand Challenge Alliance, Vol. **3**, No. 8, (1997).
- [27] L. Rezzolla, A. M. Abrahams and M. E. Rupright, Newsletter of the Grand Challenge Alliance, Vol. **4**, No. 1, (1998); Vol. **4**, No. 2, (1998).
- [28] G. B. Cook, M. F. Huq, S. A. Klasky, R. A. Matzner and M. A. Scheel, Newsletter of the Grand Challenge Alliance, Vol. **3**, No. 9, (1997); M. F. Huq, G. B. Cook, S. A. Klasky and M. A. Scheel, Newsletter of the Grand Challenge Alliance, Vol. **4**, No. 1, (1998).
- [29] C. R. Evans, Ph. D. Thesis, The University of Texas at Austin, (1984).
- [30] R. F. Stark and T. Piran, Phys. Rev. Lett. **55**, 891 (1985).
- [31] T. Nakamura, K. Oohara and Y. Kojima, Prog. Theor. Phys. Suppl. **90**, 76 (1987); T. Nakamura and K. Oohara in *Frontiers of Numerical Relativity*, C. R. Evans, L. S. Finn and D. W. Hobill Eds, Cambridge University Press, Cambridge (1989).